CHEMISTRY OF MATERIALS

ARTICLE

pubs.acs.org/cm

$Li_{1.43}[Fe^{II}_{4.43}Fe^{III}_{0.57}(HPO_3)_6]\cdot 1.5H_2O$: A Phosphite Oxoanion-Based Compound with Lithium Exchange Capability and Spin-Glass Magnetic Behavior

U-Chan Chung,[†] José L. Mesa,[*,‡] José L. Pizarro,[§] Iratxe de Meatza,[§] Miguel Bengoechea,[∥] Jesús Rodríguez Fernández,[▽] María I. Arriortua,[§] and Teófilo Rojo[*,‡,⊥]

[†]Institut de Chemie de la Matièrie Condenseé de Bordeaux, 87, Avenue Dr. Schweitzer, 33608, Pessac Cedex, France

[‡]Departamento de Química Inorgánica and [§]Departamento de Mineralogía-Petrología, Facultad de Ciencia y Tecnología, Universidad del País Vasco, Apdo. 644, E-48080 Bilbao, Spain

[∥]Departamento de Energía, CIDETEC, Paseo Miramón 196, Parque Tecnológico de San Sebastián, 20009 San Sebastián, Spain

[▽]Departamento CITIMAC, Facultad de Ciencias, Universidad de Cantabria, 39005 Santander, Spain

[⊥]CICEnergigune, Parque Tecnológico, Albert Einstein 48, 01510 miñano, Álava, Spain

Supporting Information

ABSTRACT: $Li_{1.43}[Fe^{II}_{4.43}Fe^{III}_{0.57}(HPO_3)_6]\cdot 1.5H_2O$ has been synthesized by mild hydrothermal techniques. This phase exhibits a crystal structure formed by the $[Fe^{II}_{4.43}Fe^{III}_{0.57}(HPO_3)_6]^{1.43-}$ inorganic framework with the Li^+ cations as counterions. The anionic inorganic skeleton is based on layers of FeO_6 octahedra linked along the *c*-axis through $(HPO_3)^{2-}$ oxoanions. The sheets are constructed using 12-membered rings of FeO_6 octahedra that repeat in the *ab* plane, giving rise to channels ca. 3 Å in diameter along the [100] direction in which the water molecules and Li^+ cations are located showing positional disorder. The limit of the thermal stability is ~285 °C. The IR spectrum shows the vibrational bands belonging to the phosphite groups. From the fit of the Mössbauer spectrum, in the paramagnetic state, characteristic values of the isomer shift and quadrupolar splitting for the simultaneous presence of Fe(II) and (III) cations have been obtained. From the ac-magnetic measurements, spin glass behavior was inferred, which can be attributed to the presence of both Fe(II) ($S = 2$) and Fe(III) ($S = {}^5/_2$) cations. The spin-glass-like state was confirmed by specific-heat experiments, with this phase being the first ordered transition-metal phosphite exhibiting this magnetic behavior. The existence of mobile lithium cations in the channels of $Li_{1.43}[Fe^{II}_{4.43}Fe^{III}_{0.57}(HPO_3)_6]\cdot 1.5H_2O$ was studied by impedance spectroscopy at different temperatures. The obtained Nyquist diagrams reveal two conduction processes. Electrochemical characterization was completed by cyclic voltammetry experiments and galvanostatic measurements. A reversible exchange of lithium is also observed for this compound for more than 100 galvanostatic cycles, equivalent to 12 mAh g^{-1} of sample.

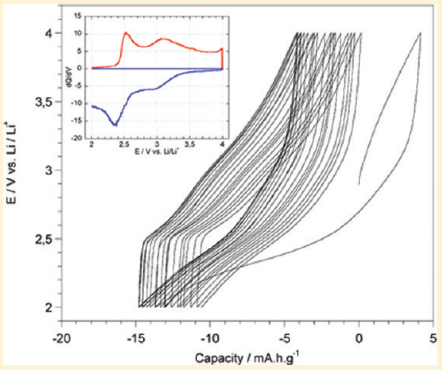

KEYWORDS: hydrothermal synthesis, crystal structure, magnetic measurements, specific heat, electrochemical properties

INTRODUCTION

Research in the area of framework solids exhibiting open structures continues to be exciting, because of their many potential applications.[1,2] Prior to the early 1980s, when the nanoporous aluminum phosphates were first reported by Flanigen and coworkers, the aluminosilictae zeolites[3] and closely related systems represented the predominant class of open-framework materials with a three-dimensional crystalline structure. Today, this investigation has given rise to a flurry of activity, resulting in many structures with different dimensionalities.[4]

Recently, several reviews dealing with organically templated phosphate, arsenate, and phosphite compounds have been published.[5] With only very few exceptions, the synthesis of these materials has been achieved by soft hydrothermal conditions in the presence of an organic molecule—generally an amine, although other organic molecules are increasingly being used. These molecules act as a structure-directing template around which the structure is built and counterbalances the charge of the anionic inorganic framework.

Referred to the phosphite oxoanion, systems containing Zn, the so-called zincophosphites, are, by far, the most numerous in either one, two, or three dimensions. However, an increasing number of structures exists where the metallic centers are occupied by open-shell transition-metal ions, thus giving rise to new magnetic phases.[5d]

Open-framework solids that have large channels and cavities have been exploited for catalysis and related studies.[5b,6] It is

Received: May 11, 2011
Revised: August 24, 2011
Published: September 13, 2011

becoming equally important to discover new solids with fascinating structures that offer new properties and applications. In this sense, lithium intercalation into the channels or cavities of these open-framework solids opens the gates to the attainment of new phases with interesting ionic conductivity properties.

Within this field, many lithium transition-metal and polyanion-based materials have been widely studied, in search of novel lithium conductors and intercalation compounds, including different structures with $(XO_4)^{n-}$ and $(X_2O_7)^{n-}$ (X = P, S, As, Mo, W).[7−9] However, to the best of our knowledge, no lithium and transition-metal compound has been obtained with the phosphite oxoanion, $(HP^{III}O_3)^{2-}$, which is an oxoanion with only three bonding oxygen atoms and a P−H group. To date, the most important work has been carried out in organically templated inorganic−organic solids;[5a,b] however, no research on lithium−iron(II,III) phosphites has been reported.

In this work, we report on the hydrothermal synthesis, the spectroscopic behavior, and the magnetic and electrochemical properties of $Li_{1.43}$ $[Fe^{II}_{4.43}Fe^{III}_{0.57}(HPO_3)_6]\cdot 1.5H_2O$, which exhibits lithium ionic conductivity and an unusual magnetic behavior. As far as we are aware, this is the first phosphite oxoanion compound showing a spin-glass-like state and reversible lithium insertion/extraction into the structure.

SYNTHESIS AND CHARACTERIZATION

$Li_{1.43}[Fe^{II}_{4.43}Fe^{III}_{0.57}(HPO_3)_6]\cdot 1.5H_2O$ has been synthesized under mild hydrothermal conditions and autogenous pressure (10−20 bar at 170 °C). The reaction mixture was prepared with 30 mL of distilled water, 19.2 mmol of H_3PO_2 acid, and 0.37 mmol of $FeCl_3\cdot 6H_2O$. Finally, $Li(OH)\cdot H_2O$ was added in an amount of 20.5 mmol, reaching a final pH value of ∼3.0. The reaction mixture was sealed in a polytetrafluoroethylene (PTFE)-lined steel pressure vessel, which was maintained at 170 °C for five days. This procedure allowed the formation of single crystals with a dark green color and good quality for the structural study by XRD.

The metal and phosphorus contents were determined by inductively coupled plasma−atomic emission spectroscopy (ICP-AES), atomic absorption spectroscopy (AAS), and inductively coupled plasma−mass spectroscopy (ICP-MS). The following results are observed:

Found: Fe, 37.4; P, 21.1; Li, 1.2.

Required; Fe, 37.6; P, 21.4; Li, 1.3.

In order to calculate the Fe(III):Fe(II) ratio, Mössbauer experiments at room temperature were carried out. The results obtained and the electroneutrality condition, together with the ICP data, allowed us to obtain the following chemical composition: $Li_{1.43}[Fe^{II}_{4.43}Fe^{III}_{0.57}(HPO_3)_6]^{III}_{0.57}\cdot 1.5H_2O$.

The density was measured by the flotation procedure in a mixture of diiodomethane (CH_2I_2) and trichloromethane (Cl_3CH), using a single crystal. The result is 3.01(4) g cm^{-3}, with the theoretical density obtained from X-ray diffraction (XRD) data being 3.137 g cm^{-3}.

The compound was characterized by XRD on a powdered sample. The diffraction maxima of its pattern were indexed using the TREOR program,[10] and the following unit-cell parameters: a = 10.2(1) Å, c = 9.2(1) Å, and γ = 120° were obtained. The study of the systematic absence of reflections pointed to the $P\bar{3}c1$ space group of the trigonal system. Starting from this data, the pattern was fitted using the pattern matching routine of the FULLPROF program,[11] confirming the purity and the high crystallinity of the sample.

CRYSTAL STRUCTURE DETERMINATION

A single crystal with dimensions of 0.51 mm × 0.03 mm × 0.03 mm was selected under a polarizing microscope and mounted with inert oil on a Mitegen micromount. Single-crystal X-ray diffraction (XRD) data were collected on an Oxford Diffraction Xcalibur2 automated diffractometer (Mo Kα radiation) equipped with a Sapphire2 CCD detector, at 100(1) K, using an Oxford Cryosystems Cryostream 700 unit. The diffractometer software[12] was used to make the Lorentz polarization and absorption corrections, taking into account the size and shape of the crystal, as well as the data reduction. The integration of the data yielded 13 713 reflections to a maximum θ angle of 30.5° (0.7 Å resolution); 863 of these reflections were unique, with an R_{int} factor of 0.0365. The number of observed reflections with $I > 2\sigma(I)$ was 818. The structure was solved by direct methods using Superflip[13a] in the $P\bar{3}c_1$ space group. All atoms belonging to the inorganic framework were located at this stage; however, the high agreement factors indicated that the crystal could be twinned. This was confirmed to be twinned by merohedry with the TwinRotMap option of PLATON.[13b] The twin element is a 180° rotation around the $\langle 1\bar{1}0\rangle$ direction, or any other equivalent representative of the left co-set decomposition of the $6/mmm$ holohedry under the $\bar{3}m1$ crystal class. The twin law ($0\bar{1}0/\bar{1}00/00\bar{1}$) was used during the refinements, and the twin volume of the second component was refined to a value of 0.379(1).

The least-squares F^2-based refinement of the structure, performed by SHELXL97,[14] allowed the location of the phosphite group hydrogen, and showed residual density inside the channels of the structure, which could be successfully modeled as water molecules and lithium cations, both positionally disordered over two mutually exclusive crystallographic sites.

All of the atoms, except the hydrogen of the phosphite group and the lithium cations, were anisotropically refined. The hydrogen of the phosphite group was restrained to be equidistant to the three oxygen atoms of the group, and was assigned a fixed isotropic displacement parameter with a value equal to 1.2U_{eq} of the parent P atom. The two lithium atoms were constrained to have the same isotropic displacement parameter, but their occupancy factors (as well as those of the water molecules) were freely refined.

The final R-factors were $R1$ = 0.0167 and $wR2$ = 0.0450, with R-factors of $R1$ = 0.0177 and $wR2$ = 0.0451 for all data. The structure factor parameters have been deposited at the Cambridge Crystallographic Data Centre (CCDC File No. 824501, http://www.ccdc.cam.ac.uk). All drawings were performed with the ATOMS program.[15] Crystallographic data are given in Table 1.

PHYSICOCHEMICAL CHARACTERIZATION TECHNIQUES

Thermogravimetric analysis was carried out in a Model DSC 2960 simultaneous DSC−TGA instrument, under a synthetic air atmosphere. A crucible with ca. 20 mg of sample was heated at a rate of 5 °C min^{-1} from room temperature to 800 °C. Temperature-dependent X-ray diffraction (XRD) study on powdered sample was performed in a Philips X'Pert automatic diffractometer (Cu Kα radiation) equipped with a variable-temperature Anton Paar HTK16 Pt stage. The patterns were recorded from 30 °C to 810 °C in intervals of 15 °C in the range of 5° ≤ 2θ ≤ 38.5° with an integration time of 1 s per 0.03° step. The IR spectrum was recorded using KBr pellets, within the

dx.doi.org/10.1021/cm201337g |Chem. Mater. 2011, 23, 4317–4330

Table 1. Details of the Crystal Data, Structural Resolution, and Refinement Procedure for $Li_{1.43}[Fe^{II}_{4.43}Fe^{III}_{0.57}(HPO_3)_6]\cdot 1.5H_2O$

formula	$Li_{1.43}[Fe^{II}_{4.43}Fe^{III}_{0.57}(HPO_3)_6]\cdot 1.5H_2O$
molecular weight	792.39 g mol^{-1}
crystal system	trigonal
space group (number)	$P\bar{3}c1$ (165)
a	10.2568(2) Å
c	9.2086(2) Å
V	838.97(3) Å^3
Z	2
ρ_{obs}	3.01(4) g cm^{-3}
ρ_{calc}	3.137 g cm^{-3}
$F(000)$	771.6
	Collection data
temperature	100(1) K
diffractometer	Oxford Diffraction Xcalibur2
μ	4.899 mm^{-1}
radiation, λ(Mo Kα)	0.71073 Å
reflection collected/ unique	13713/863 [R_{int}= 0.0365]
range θ	3.19°−30.48°
interval h, k, l	$-14 \le h \le 14$, $-14 \le k \le 14$, $-13 \le l \le 13$
	Refinement
number of data/restraints/ parameters	863/4/65
R factors [obs. data][a]	$R1$ = 0.0164, $wR2$ = 0.0436
R factors [all data][a]	$R1$ = 0.0174, $wR2$ = 0.0438
max. electronic residual density	0.526 e Å^{-3}
min of electronic residual density	−0.303 e Å^{-3}
goodness of fit, GOF	1.133

[a] $R1 = \frac{\Sigma\left||F_0| - |F_c|\right|}{\Sigma|F_0|}$; $wR2 = \frac{\Sigma w\left(|F_0| - |F_c|\right)^2}{\Sigma w|F_0|^2}$, with

$w = \frac{1}{\sigma^2|F_0|^2 + (xp)^2}$, $p = \frac{\max|F_0|^2 + 2|F_c|^2}{3}$, and x = 0.0238.

400−4000 cm^{-1} region on a Mattson FTIR 1000 spectrometer. The absorption spectra from 210 nm to 2000 nm, measured by diffuse reflectance, were obtained with a Cary Model 5000 UV−vis−IR spectrometer. The Mössbauer measurements were performed in the paramagnetic state at room temperature using a source of ^{57}Co−Rh and calibrating the velocity with α-Fe. Magnetic susceptibility measurements (dc) were performed in an applied field of 1 KOe over the temperature range of 2.0−300 K, using a Quantum Design MPMS superconducting quantum interference device magnetometer. Data were collected after both zero field cooling and field cooling of the sample. Magnetization was measured as a function of field in a standard Quantum Design PPMS system, the data were collected in the range $-85 \le H/\text{kOe} \le 85$ at different temperatures between 2 and 100 K after cooling the sample in a zero field. For the ac magnetic susceptibility, a PPMS system with an alternate excitation field of 4 Oe and frequencies between 10 and 10^4 Hz was used. The heat capacity was also measured in a PPMS device using a two-τ model; the sample was a plate 0.4 mm thick and 8 mg in weight, obtained by compressing the original powder. The conductivity of the sample was analyzed by electrochemical impedance spectroscopy measurements up to 190 °C on square-shaped pellets with Cu electrodes, using a Solartron 1260 Frequency Response Analyzer.

Cyclic voltammetry and galvanostatic tests were conducted on Swagelok-type cells assembled in an Ar-filled glovebox (LabMaster 130, MBraun), with lithium metal foil as the negative electrode. A powder mixture of $Li_{1.43}[Fe^{II}_{4.43}Fe^{III}_{0.57}(HPO_3)_6]\cdot 1.5H_2O$, carbon black (for electrical conductivity), and poly(vinylidene fluoride) (PVDF) as binder, in a 61:30:9 weight ratio, was compressed as an 8-mm-diameter disk (<0.3 mm thick) and used as the positive electrode. A glass microfiber sheet soaked in a solution of 1 M $LiPF_6$ in EC:DMC (1:1 w/w) (Merck) as the electrolyte was placed between the two electrodes. Measurements were carried out using a Biologic Multichannel Potentiostat Galvanostat (MPG) system.

RESULTS AND DISCUSSION

Crystal Structure Description. Atomic coordinates and selected bond distances and angles are listed in Tables 2 and 3, respectively.

The lithium and water content per unit formula were refined to values of 1.41(3) and 1.47(3), respectively, so that the crystallographically determined formula, $Li_{1.41}[Fe_5(HPO_3)_6]\cdot 1.5H_2O$, agrees nicely with that obtained with the other analytical techniques, $Li_{1.43}[Fe^{II}_{4.43}Fe^{III}_{0.57}(HPO_3)_6]\cdot 1.5H_2O$.

This phase has a crystal structure formed by sheets of FeO_6 octahedra linked along crystallographic direction c via phosphite groups (see Figure 1). The Fe ions occupy two different special sites with a relation Fe(1):Fe(2) of 3:2, whereas the P atoms occupy general positions. In the FeO_6 octahedra, the Fe−O bond distances range from 2.032(2) Å to 2.186(2) Å, while the bond angles are between 77.45(5)° and 103.17(5)° for the *cis* structure and between 163.49(6)° and 177.55(9)° for the *trans* structure. The phosphite group presents P−O bond distances between 1.521(2) Å and 1.539(2) Å, and a P−H distance of 1.27(4) Å, while the O−P−O bond angles range from 109.96(8)° to 114.12(9)°. The sheets are formed by 12-membered rings of FeO_6 octahedra that repeat in the *ab* plane. Each ring is formed by six octahedra of Fe(1) and the other six of Fe(2). Linked to each ring by the most interior oxygens of each level, there are six phosphite groups (see Figure 2). The coincidence of the rings along the [001] direction gives rise to 12-membered ring channels ca. 3 Å in diameter (see Figure 3). The water molecules and lithium cations, showing a positional disorder, are located in these channels.

The two crystallographic independent Fe(1) and Fe(2) cations exhibit octahedral coordination, each one surrounded by six oxygen atoms. In the $Fe(1)O_6$ and $Fe(2)O_6$ octahedra the Fe−O bond distances range from 2.032(2) Å to 2.186(2) Å and from 2.134(2) Å to 2.141(2) Å. The *cis*-bond angles are in the 77.49(6)°−100.68(6)° and 77.45(5)°−103.17(5)° ranges, whereas the *trans*-bond angles have mean values of 170.14(6)° and 163.49(6)°

dx.doi.org/10.1021/cm201337g |*Chem. Mater.* 2011, 23, 4317–4330

Table 2. Wyckoff Positions, Atomic Coordinates, Equivalent Temperature Factors, and Occupancy Factors for $Li_{1.43}[Fe^{II}_{4.43}Fe^{III}_{0.57}(HPO_3)_6]\cdot 1.5H_2O$

	Positions						
atom	multiplicity, Wyckoff letter	site symmetry	x	y	z	equivalent temperature factor, U_{eq}[a] (Å^3)	occupancy factor, OF
Fe(1)	6f	0.2	0.38334(4)	0.38334(4)	0.25	0.0076(1)	1.0
Fe(2)	4d	3	0.66667	0.33333	0.33295(6)	0.0061(1)	1.0
P(1)	12g	1	0.41005(5)	0.11556(5)	0.08911(6)	0.0073(1)	1.0
H(1P)	12g	1	0.317(2)	−0.026(3)	0.090(2)	0.0090	1.0
O(1)	12g	1	0.3201(2)	0.1870(2)	0.1435(2)	0.0138(4)	1.0
O(2)	12g	1	0.5418(2)	0.1477(2)	0.1902(2)	0.0091(3)	1.0
O(3)	12g	1	0.4669(2)	0.1579(2)	−0.0680(2)	0.0107(4)	1.0
O(1W)	4c	3	0.0	0.0	0.079(2)	0.051(4)	0.45(5)
O(2W)	2a	32	0.0	0.0	0.25000	0.083(10)	0.54(2)
Li(1)	6f	0.2	0.110(6)	0.110(6)	0.25000	0.043(11)	0.16(4)
Li(2)	12g	1	0.047(5)	0.096(5)	0.152(5)	0.043(11)	0.16(2)

[a] $U_{eq} = {}^1/_3\{(aa^*)^2[U_{11} + U_{22} + U_{33} + 2\cos\alpha(U_{12} + U_{13} - U_{23})]\}$.

Table 3. Selected Bond Distances and Bond Angles for $Li_{1.43}[Fe^{II}_{4.43}Fe^{III}_{0.57}(HPO_3)_6]\cdot 1.5H_2O$[a]

$Fe(1)O_6$ Octahedron

Fe(1)	O(1)	O(1)^i	O(2)^{ii}	O(2)^{iii}	O(3)^{iv}	O(3)^v
O(3)^v	90.62(6)°	90.99(6)°	100.69(6)°	77.49(6)°	177.55(9)°	2.186(2) Å
O(3)^{iv}	90.99(6)°	90.62(6)°	77.49(6)°	100.68(6)°	2.186(2) Å	
O(2)^{iii}	89.17(6)°	166.43(6)°	86.01(8)°	2.086(2) Å		
O(2)^{ii}	166.43(6)°	89.17(6)°	2.086(2) Å			
O(1)^i	98.21(9)°	2.032(2) Å				
O(1)	2.032(2) Å					

$Fe(2)O_6$ Octahedron

Fe(2)	O(2)	O(2)^{ii}	O(2)^v	O(3)	O(3)^{ii}	O(3)^v
O(3)^v	92.62(6)°	163.49(6)°	77.45(5)°	103.17(5)°	103.17(5)°	2.141(2) Å
O(3)^{viii}	163.49(6)°	77.45(5)°	92.62(6)°	103.17(5)°	2.141(2) Å	
O(3)^{vii}	77.45(5)°	92.62(6)°	163.49(6)°	2.141(2) Å		
O(2)^{iii}	86.04(6)°	86.04(6)°	2.134(1) Å			
O(2)^{vi}	86.04(6)°	2.134(1) Å				
O(2)	2.134(1) Å					

HPO_3 Tetrahedron

P(1)	O(1)	O(2)	O(3)^{vi}	H
H(1P)	105(1)°	108(1)°	106(1)°	1.27(4) Å
O(3)	114.12(9)°	109.96(8)°	1.539(2) Å	
O(2)	112.20(9)°	1.535(2) Å		
O(1)	1.521(2) Å			

[a] Symmetry codes: $i = y, x, -z + {}^1/_2$; $ii = -x + 1, -x + y + 1, -z + {}^1/_2$; $iii = -x + y + 1, -x + 1, z$; $iv = x - y, x, -z$; $v = x, x - y, z + {}^1/_2$; $vi = -y + 1, x - y, z$; $vii = -x + y + 1, y, z + {}^1/_2$; $viii = -y + 1, -x + 1, z + {}^1/_2$.

for $Fe(1)O_6$ and $Fe(2)O_6$ octahedra, respectively. The distortions of the $Fe(1)O_6$ and $Fe(2)O_6$ polyhedra have been calculated using the Muetterties and Guggenberger description.[16] The values of the distortion (Δ) between the ideal geometries, octahedron ($\Delta = 0$) and trigonal prism ($\Delta = 1$), for every octahedron are 0.23, and 0.18, respectively. These values indicate an appreciable deviation from the ideal octahedral geometry.

The water molecules are located in the center of the channels, disordered over two sites [(O1W) and (O2W)] with occupation factors of 0.45(2) and 0.55(3), respectively. They are both at the hydrogen-bond distance of the O(1) oxygen atoms that line the inside wall of the channels: O(1W) at 2.917(4) Å of three O(1) atoms, and 3.14(2) Å of O(1W); and O(2W) at 3.021(2)Å of six O(1) atoms (see Figure 4 and Table S1 in the Supporting Information). The Li cations are placed around the water molecules, between them and the channel walls, disordered over two sites, Li(1) and Li(2), with occupation factors of 0.17(2) and 0.16(2), respectively. The Li(1) site shows a distorted tetrahedral LiO_4 environment, coordinated to two water molecules at the O(1W) site and two O(1) oxygen atoms, with Li−O distances in the range of 1.93(4)−2.13(4) Å. On the other hand, the Li(2) site shows much longer coordination distances to only two water molecules, 2.29(6) and 2.48(5) Å. (See Figure 5 and Table S2 in the Supporting Information).

Thermal Behavior. The thermogravimetric measurement exhibits a rapid mass loss of ∼2% between room temperature and 220 °C due to the elimination of the water molecules inside the channels. From this temperature and up to 345 °C, the percentage of mass in the thermogravimetric (TG) curve is constant. Above this temperature, the experiments show a moderate increase in mass. In the 315 and 335 °C range, the DTA curve shows an exothermic peak, which corresponds to the Fe^{2+}-to-Fe^{3+} oxidation process. The oxidation from phosphite to phosphate occurs in the 415−425 °C range, with a maximum observed in the DTA curve and a mass gain of ∼25%. The exothermic peak observed at temperatures above 425 °C corresponds to a process in which the crystallization of the inorganic residues occurs. These have been characterized by powder XRD data. The hematite (Fe_2O_3) [$R\bar{3}c$, a = 5.032 Å, c = 13.733 Å][17a] and the trigonal $Fe(PO_4)$ phase [$P3_121$, a = 5.027 Å, c = 11.234 Å][17b] were identified. Furthermore, the residue contains $LiFe(P_2O_7)$ [$P2_1$, a = 4.825 Å, b = 8.079 Å, c = 6.938 Å, β = 109.38°],[17c] which explains the considerable increase of the final mass observed in the TG curve at the

dx.doi.org/10.1021/cm201337g |Chem. Mater. 2011, 23, 4317–4330

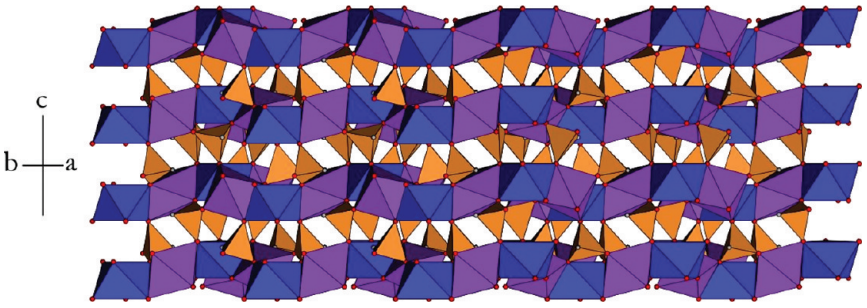

Figure 1. View of the octahedral sheets linked by phosphite groups for $Li_{1.43}[Fe^{II}_{4.43}Fe^{III}_{0.57}(HPO_3)_6]\cdot 1.5H_2O$.

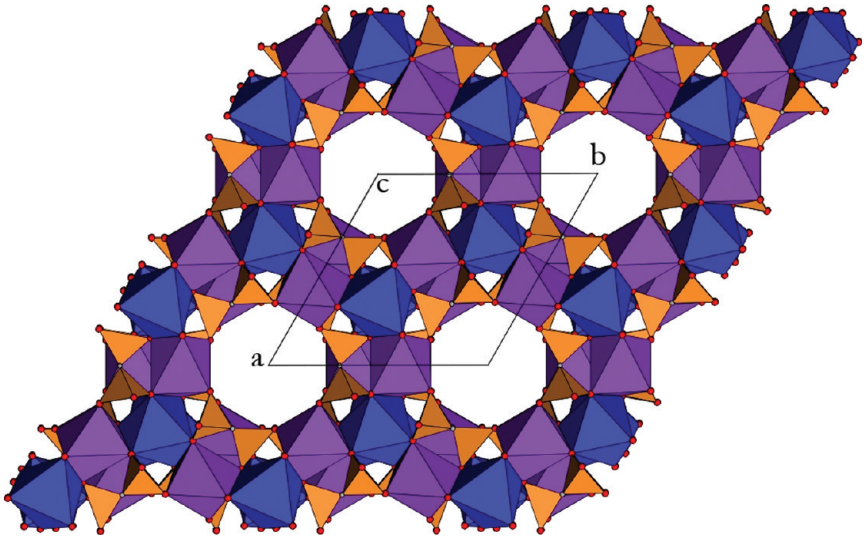

Figure 2. View along the *c*-axis of the crystal structure, where the channels along the [001] direction can be seen.

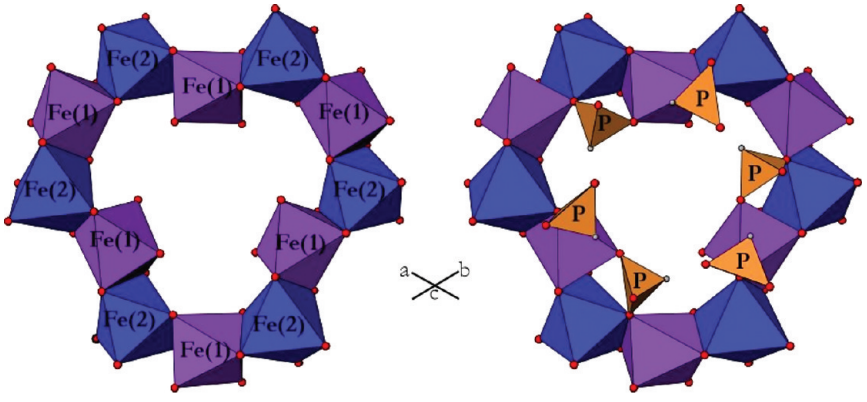

Figure 3. Rings constructed by twelve octahedra; the disposition of the $Fe(1)O_6$ and $Fe(2)O_6$ octahedra is shown on the left-hand side, and the connectivity of the phosphite groups to the rings is reflected in the image on the right-hand side.

higher temperature measured (800 °C), which corresponds to a mass gain of ∼20%.

Temperature-dependent XRD experiments show that the thermal stability limit for the compound is 285 °C, which is the temperature at which the destruction of the crystal structure begins. After that temperature range, from 315 °C to 390 °C, no diffraction maxima appear (see Figure 6). At temperatures above 390 °C, the presence of different residual phases, corresponding to those observed in the TG measurements, were observed. The hematite crystallizes in the temperature range from 390 °C to 510 °C and disappears at 780 °C, while $Fe(PO_4)$ crystallizes between 555 °C and 630 °C, and the lithium−iron(III) pyrophosphates crystallize between 465 °C and 690 °C.

Infrared (IR), Ultraviolet-Visible Light (UV−Vis), and Mössbauer Spectroscopies. The IR spectrum (Figure 7) shows a broad band centered at 3490 cm^{-1} that corresponds to the

dx.doi.org/10.1021/cm201337g |*Chem. Mater.* 2011, 23, 4317–4330

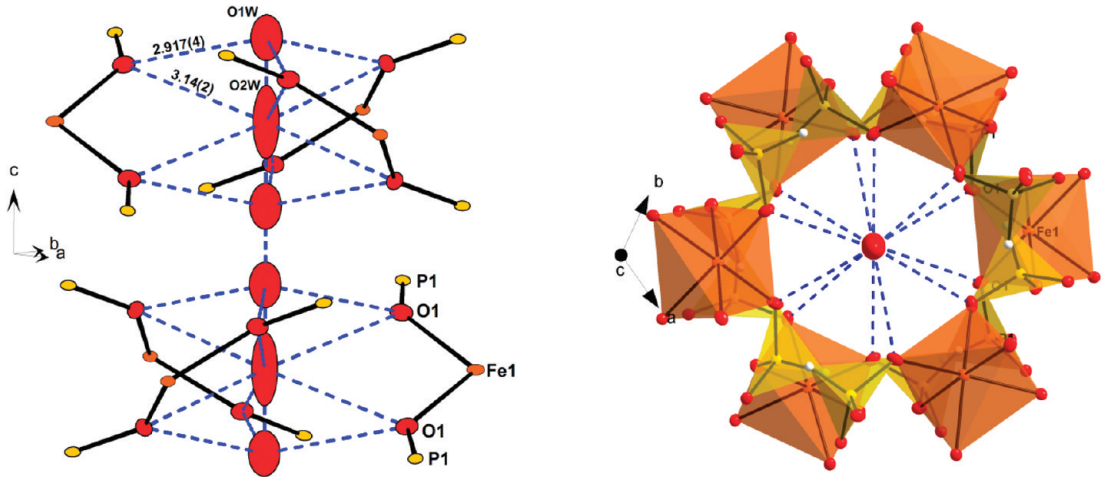

Figure 4. View perpendicular to (left) and along (right) the *c*-axis, of the water molecules at the center of the channels along the [001] direction: (left) perpendicular to the *c*-axis and (right) along the *c*-axis. The Li cations have been omitted for the sake of clarity.

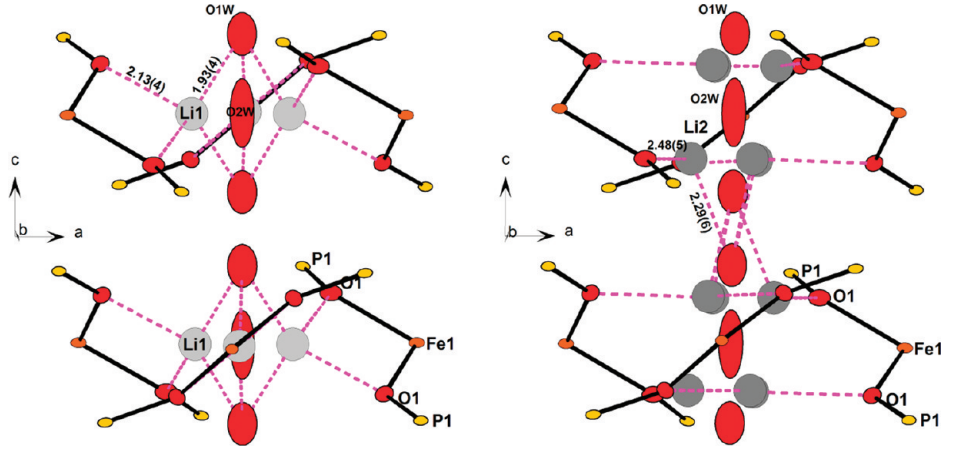

Figure 5. View perpendicular to the *c*-axis of the coordination details around the (left) Li1 sites and (right) Li2 sites.

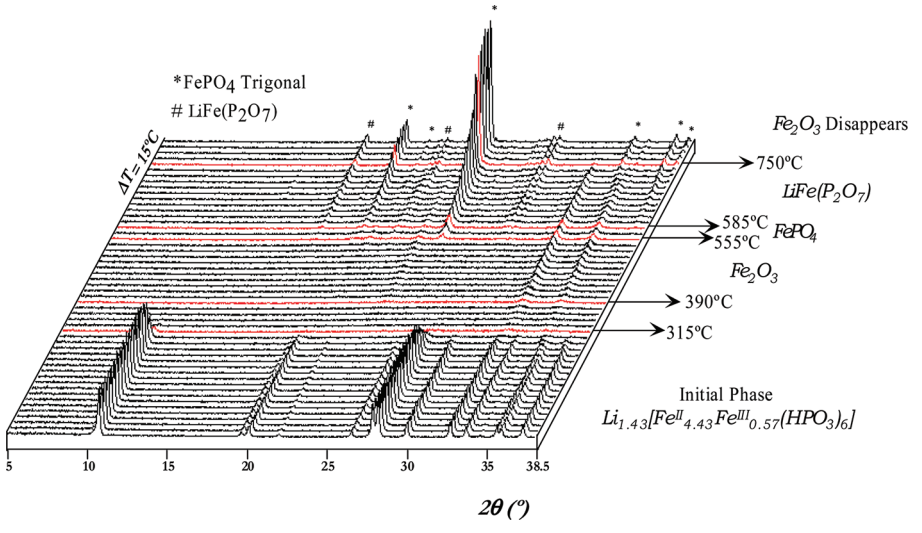

Figure 6. Thermodiffractograms for $Li_{1.43}[Fe^{II}_{4.43}Fe^{III}_{0.57}(HPO_3)_6]\cdot 1.5H_2O$.

stretching vibration of the water molecules, ν(H−O−H). The bending mode of these molecules, δ(H−O−H), is detected at 1600 cm^{-1}.[18a] Besides the IR spectrum shows the stretching and deformation modes of the P−H bond at ∼2500 and 1045 cm^{-1},

dx.doi.org/10.1021/cm201337g |*Chem. Mater.* 2011, 23, 4317–4330

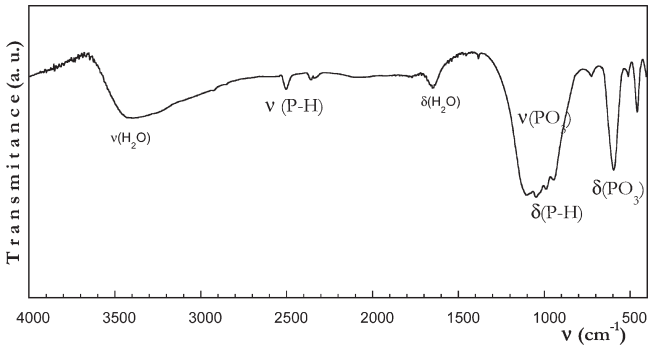

Figure 7. Infrared (IR) spectrum of $Li_{1.43}[Fe^{II}_{4.43}Fe^{III}_{0.57}(HPO_3)_6]\cdot 1.5H_2O$.

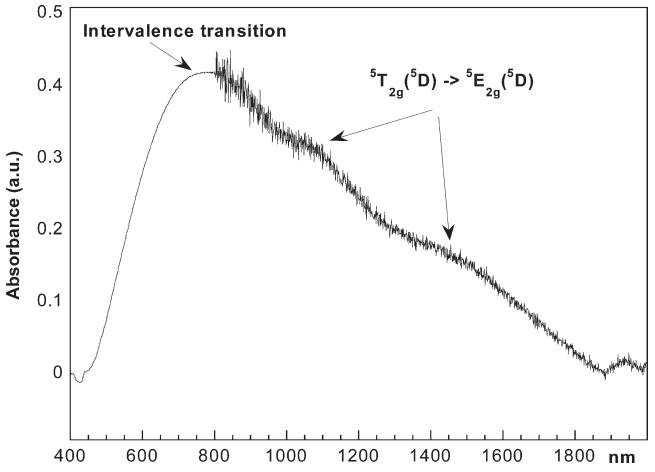

Figure 8. Ultraviolet−visible light (UV-Vis) spectrum for $Li_{1.43}[Fe^{II}_{4.43}Fe^{III}_{0.57}(HPO_3)_6]\cdot 1.5H_2O$.

respectively. The bands corresponding to the symmetric (ν_s) and antisymmetric (ν_{as}) stretching vibrational modes of the $(PO_3)^{2-}$ groups appear at 930 and 1115 cm^{-1}, whereas the symmetric (δ_s) and antisymmetric (δ_{as}) deformation modes are centered at 450 and 590 cm^{-1}.[18b]

The diffuse reflectance spectrum has been registered at room temperature in the 200−2000 nm range, and it shows the presence of three bands (see Figure 8). One broad band located between 770 nm and 820 nm that corresponds to a Fe(II)−Fe(III) intervalence transition[19] is observed. This fact can be attributed to the existence of shared oxygen atoms between the metallic cations. The weak bands centered at ∼1050 and ∼1550 nm correspond to the transitions from the split $^5T_{2g}(^5D)$ ground state to the $^5E_{2g}(^5D)$ excited level of the Fe^{2+} cations.[20] The Dq parameter has been calculated from the mean positions of these two transitions and the obtained value being 820 cm^{-1}, which is in good agreement with those obtained for similar phases.[21]

In the Mössbauer spectrum, shown in Figure 9, the presence of three components is observed: two doublets, corresponding to Fe^{2+} cations, and a third doublet, corresponding to Fe^{3+} cations. The spectrum was fitted with the NORMOS program.[22] According to the structural data, the Fe ions occupy two crystallographically independent sites with a multiplicity ratio of 3:2 for Fe(1):Fe(2), and a substitution of Fe^{2+} by Fe^{3+} occurs in both crystallographic sites of the Fe cations. The relative quantity of Fe^{2+} and Fe^{3+} was calculated from the relative spectral areas. The

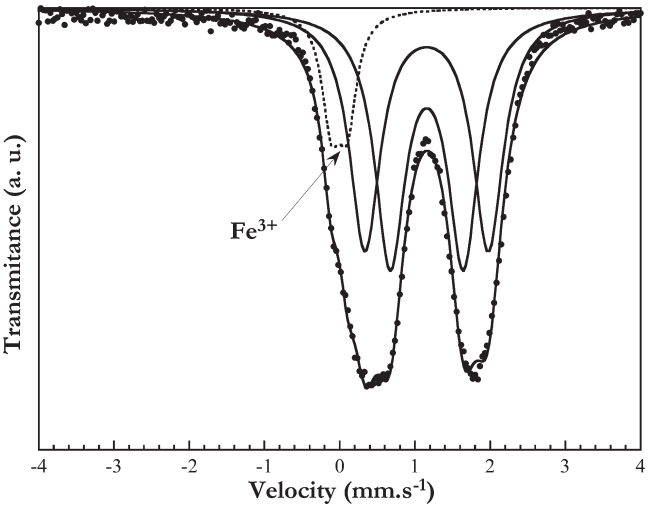

Figure 9. Mössbauer spectrum at room temperature for $Li_{1.43}[Fe^{II}_{4.43}Fe^{III}_{0.57}(HPO_3)_6]\cdot 1.5H_2O$.

Table 4. Values of the Isomer Shift (δ), Quadrupolar Splitting (ΔE), and Iron Percentages, Obtained through the Fit of the Spectrum, Assigned to Every Crystallographic Position for $Li_{1.43}[Fe^{II}_{4.43}Fe^{III}_{0.57}(HPO_3)_6]\cdot 1.5H_2O$

site	δ (mm s^{-1})	ΔE (mm s^{-1})	% Fe
$Fe^{2+}(1)$	1.272(2)	1.643(7)	42.68(2)
$Fe^{2+}(2)$	1.269(1)	0.977(6)	45.92(1)
Fe^{3+}	0.109(3)	0.214(5)	11.40(1)

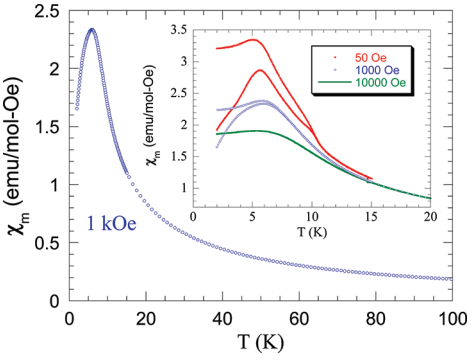

Figure 10. Thermal evolution of the susceptibility for $Li_{1.43}[Fe^{II}_{4.43}Fe^{III}_{0.57}(HPO_3)_6]\cdot 1.5H_2O$ measured at 1 kOe. The inset shows the zero field cooling−field cooling (ZFC-FC) susceptibility at different magnetic fields.

values of the isomer shifts and quadrupolar splitting are in the range observed for these cations,[23] and are shown, together with the relative quantities of Fe^{2+} and Fe^{3+}, in Table 4.

Magnetic Behavior. The magnetic susceptibility measurements have been performed on a powdered sample in the temperature range of 2−300 K, under applied magnetic fields of 1 kOe. The results are given in Figure 10.

The thermal evolution of the χ_m vs T curve shows a maximum, at ∼6 K; above this temperature, the susceptibility continuously decreases with increasing temperature, suggesting a paramagnetic behavior. Indeed, the inverse of the magnetic susceptibility

dx.doi.org/10.1021/cm201337g |Chem. Mater. 2011, 23, 4317–4330

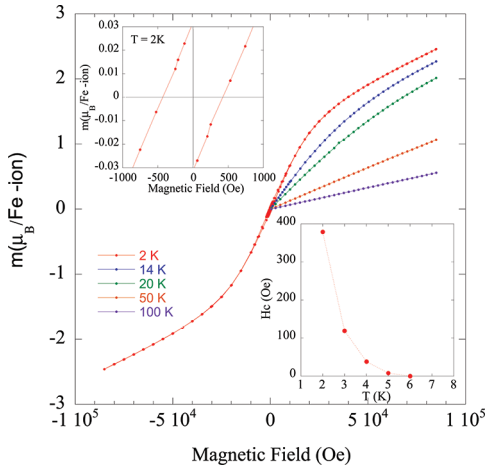

Figure 11. Magnetization versus magnetic field for $Li_{1.43}[Fe^{II}_{4.43}Fe^{III}_{0.57}(HPO_3)_6]\cdot 1.5H_2O$. The upper inset shows an enlargement of the hysteresis loop at $T = 2$ K around the origin. The lower inset shows the evolution of the coercive field with the temperature.

follows a perfect Curie−Weiss law above 15 K (see the Supporting Information), using a value of $\mu_{eff} = 5.5\ \mu_B$ as the paramagnetic effective moment and $\theta_p = -4.1$ K as the paramagnetic Curie temperature.

In order to obtain a more-complete picture of the magnetic behavior, ZFC and FC magnetic susceptibility measurements were carried out under different magnetic fields. ZFC-FC curves at some selected magnetic fields are depicted in the inset of Figure 11. First, at 50 Oe, after the maximum at 6 K, the curves exhibit a small kink at 10 K. This kick disappears for fields higher than 200 Oe. Second, the ZFC-FC curves show a small irreversibility below 10 K. This irreversibility becomes larger at temperatures below 6 K. The irreversibility that initiates at 10 K disappears for small magnetic fields (200 Oe), whereas below 6 K, the irreversibility is stronger against the field, although continuously decreases with increasing magnetic field, disappearing at ∼10 kOe.

Although the peak in the magnetic susceptibility is characteristic of either antiferromagnetic or spin-glass behavior, the existence of clear irreversibility below 6 K is more compatible with the second one. In order to confirm the existence of the spin-glass transition, ac susceptibility measurements have been performed. The real (χ') and imaginary (χ'') components of the susceptibility have been measured at 4 Oe and different frequencies between 10 and 10 000 Hz (see Figure 12). The real component shows a well-defined peak at ∼6 K and a small shoulder at 10 K, which is in excellent agreement with the dc susceptibility at low fields. These two transitions give rise to two small peaks in the imaginary component (see Figure 12b). The most important feature is that the transition at 6 K is frequency-dependent, as can be clearly observed in χ' and χ'' (see Figure 12). The peak height of χ' decreases and the position of the maximum shifts to higher temperatures with increasing frequency. These dependences are consistent with a cooperative freezing of individual magnetic moments, as in spin glasses, where the frozen state occurs at temperatures below that of the maximum of χ'.

In the frozen state, we can define a relaxation time τ_m (T_f), which corresponds to the measured time ($\tau_m = 1/\nu$) in ac susceptibility measurements. The freezing temperature (T_f) is

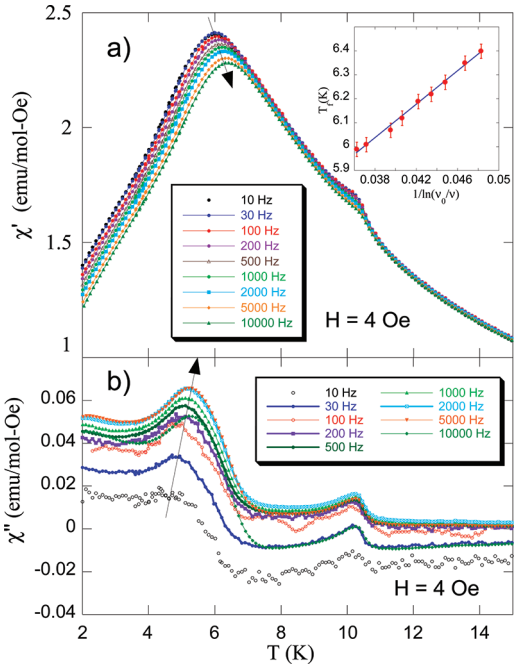

Figure 12. Evolution with temperature of the ac magnetic susceptibility measured (a) in phase (χ') and (b) out of phase (χ''). The arrows show the increase of the temperature of the maximum with the increasing frequency. The inset shows the fitting to the Vogel−Fulcher law (see text).

defined as that corresponding to the maximum in χ'. In order to analyze the temperature dependence of τ_m, we have used the Vogel−Fulcher law:[24]

$$\tau_m = \tau_0 \exp\left[\frac{E_a}{k_B(T_f - T_0)}\right]$$

in which τ_m diverges at a temperature T_0, which is smaller than the freezing temperature T_f. We should notice that, in $Li_{1.43}[Fe^{II}_{4.43}Fe^{III}_{0.57}(HPO_3)_6]\cdot 1.5H_2O$, the frequency shifts of the maximum in the susceptibility, assuming the variation of χ' to be a Gaussian function around T_f, yield the ratio $\Delta T_f/[T_f\Delta(\log \nu)] = 0.023$, which is in good agreement with the values found in canonical semiconductor spin glasses,[25,26] as well as those recently reported for some insulating spin glasses.[27] In accordance with the Vogel−Fulcher law rewritten in term of frequency, T_f is plotted again $[\ln(\nu_0/\nu)]^{-1}$ in the inset of Figure 10a with $\nu_0 = \tau_0^{-1} = 10^{13}$ Hz.[24] The experimental data follow this law well, with fitting parameters of $T_0 = 4.71$ K and an activation energy of $E_a = 35$ K. These values are similar to those usually encounted in spin glasses.[24,26,27]

Regarding the above procedure that we have followed, it should be stressed that, although T_f is usually defined as the maximum of χ', this is strictly not correct and must be defined as the temperature corresponding to the onset of the magnetic irreversibility. In addition, because spin-glass freezing is a phase transition and, as such, must be characterized by critical exponents, the more-appropriate law near the spin-glass transition is the power law. In any case, our analysis is sufficient to identify the transition at 6 K as being due to the spin-glass behavior, even though we could not go to the lower time scales needed to determine the dynamic critical exponent. All of these aspects have been discussed in detail by Mauger et al.[25]

dx.doi.org/10.1021/cm201337g |Chem. Mater. 2011, 23, 4317–4330

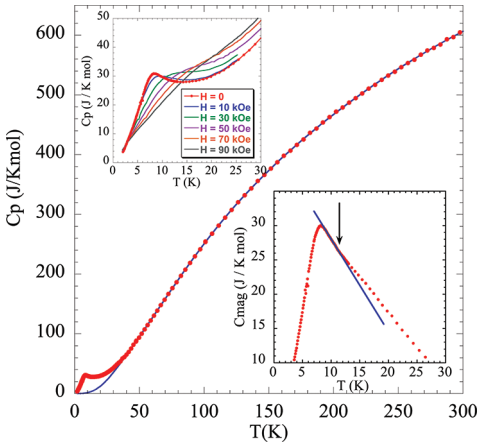

Figure 13. Specific heat measurements in the temperature range of 2−300 K. The upper inset shows the dependence of *Cp* with the magnetic field. The thermal dependence of the magnetic contribution (Cp_{mag}) is shown in the lower inset.

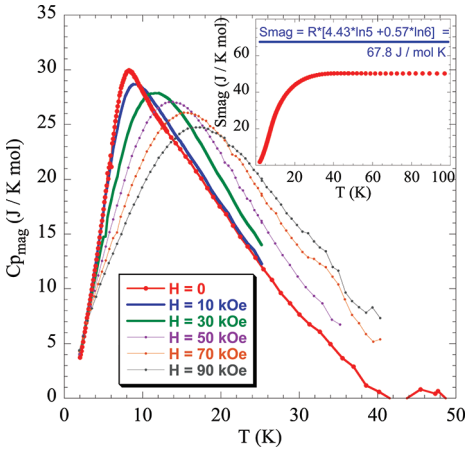

Figure 14. Temperature dependence of the magnetic specific heat (Cp_{mag}) under different magnetic fields. The inset shows the thermal dependence of the magnetic entropy (S_{mag}); the horizontal solid line represents the theoretical value of S_{mag}.

The specific-heat data between 2 K and 200 K are shown in Figure 13. The heat-capacity measurements exhibit a magnetic peak at ∼8.3 K. The temperature at which this peak appears is larger than that obtained from the magnetic susceptibility measurements (6 K). The relatively rounded magnetic peak, together with the ratio between the temperature of the peak at *Cp* and at the peak in the magnetic susceptibility ($T_{max}(Cp)/T_{max}(\chi)$ = 1.4) are fingerprints of a spin-glass transition.[26c]

The strong increase of *Cp* at higher temperatures is due to the lattice contribution (Cp_{pho}). In order to determine Cp_{pho}, we fitted the experimental data above the magnetic transition to the Debye model; however, a large difference between both the theoretical and experimental data was observed. The reason of such discrepancy can be attributed to the presence in the unit cell of atoms such as Fe and P with higher masses than those of the O and H atoms. Therefore, more than one phonon spectrum can be present in the compound. For this reason, using the same criteria as that used in $Co_2(OH)PO_4$,[28] we determine Cp_{pho} using the Debye model, which has three Debye temperatures (the minimum number of free parameters that will allow us to fit the experimental data). In this way, if the number of atoms in the unit cell is *N*, we suppose n_1 atoms with a Debye temperature θ_1, n_2 atoms with a Debye temperature θ_2, and $n_3 = (N - n_1 - n_2)$ atoms with a Debye temperature θ_3. Therefore, there are five free parameters, namely, n_1, n_2, θ_1, θ_2, and θ_3. The best fitting is obtained for n_1= 5, θ_1= 192 K, n_2= 14.73, θ_2 = 500 K, and θ_3 = 1444 K. The good quality of the fit (see the continuous line in Figure 13) allows us to consider that this phenomenological model determines the phonon contribution reasonably well. The magnetic contribution was calculated as $Cp_{mag} = Cp - Cp_{pho}$, and has a triangular shape, extending up to 40 K (see Figures 13 (inset at bottom) and 14). It is interesting to note the small change of slope at temperature close to the maximum (see the lower inset of Figure 11, which could correspond to the small magnetic transition observed in the susceptibility at ∼10 K.

The effect of the magnetic fields on *Cp* has been also studied. With increasing field, the maximum becomes more rounded and shifts to higher temperatures (see the upper inset in Figure 13). This effect is clearly observed in the magnetic contribution (see Figure 14, where the maximum shifts from 8.3 K to 17 K when the field increases from 0 T to 9 T).

The thermal evolution of the magnetic entropy is shown in the inset of Figure 14. The entropy tends to saturate at ∼35 K, which is well above the magnetic transitions, due to the existence of a short-range order magnetic interactions. The value at saturation is 50.3 J/(mol K), which is lower than the expected value (67.8 J/(mol K)) for a system with 4.43 Fe(II) cations with $S = 2$ and 0.57 Fe(III) cations with $S = {}^5/_2$. A small reduction of the experimental entropy has been observed in other Fe materials;[29] however, in this compound, the reduction is significantly larger. This feature could be related to the spin-glass state at low temperatures, which has intrinsic disorder; therefore, below 2 K, there should be residual magnetic entropy, which should be added to our experimental values.

From the magnetic and the specific-heat measurements, it is possible to deduce a spin-glass behavior below 6 K for this compound. This result could be due to the simultaneous but random presence of Fe(II) and Fe(III) cations in this phase, which gives rise to the competing interactions. Both randomness and competing interactions lead to spin frustration, ultimately resulting in the spin-glass state. The origin to the anomaly at10 K currently is not clear: it could be due to a "weak" ferromagnetic transition, as a precursor of the spin-glass state, or it could be due to a ferromagnetic impurity (<1%) that is not detected via XRD.

Impedance Spectroscopy. Given the ideal chemical and structural conditions for ionic conduction in this phase—that is, the existence of wide 12-membered ring channels in the structure and the presence of lithium cations in these channels—a study by impedance spectroscopy was carried out. Low conductivity values (<10^{-9} S cm^{-1}) were observed in the sample below 120 °C. At higher temperatures, however, two conduction processes can be distinguished for $Li_{1.43}[Fe^{II}_{4.43}Fe^{III}_{0.57}(HPO_3)_6]$, as two semicircles in the Nyquist diagrams (see Figure 15). Thus, the experimental data were fitted to a model formed by a resistance (R_s) due to the experimental setup (electrodes, wires, sample holder) and two equivalent circuits (representing one process each), consisting of a resistance (R_n) and a constant phase element (CPE_n) (see Figure 16). Conductivity at different temperatures was consequently calculated for each process, as well as corresponding capacitance values from the CPE data (see Table 5). Taking into account the obtained capacitance values and following the classification

dx.doi.org/10.1021/cm201337g |*Chem. Mater.* 2011, 23, 4317–4330

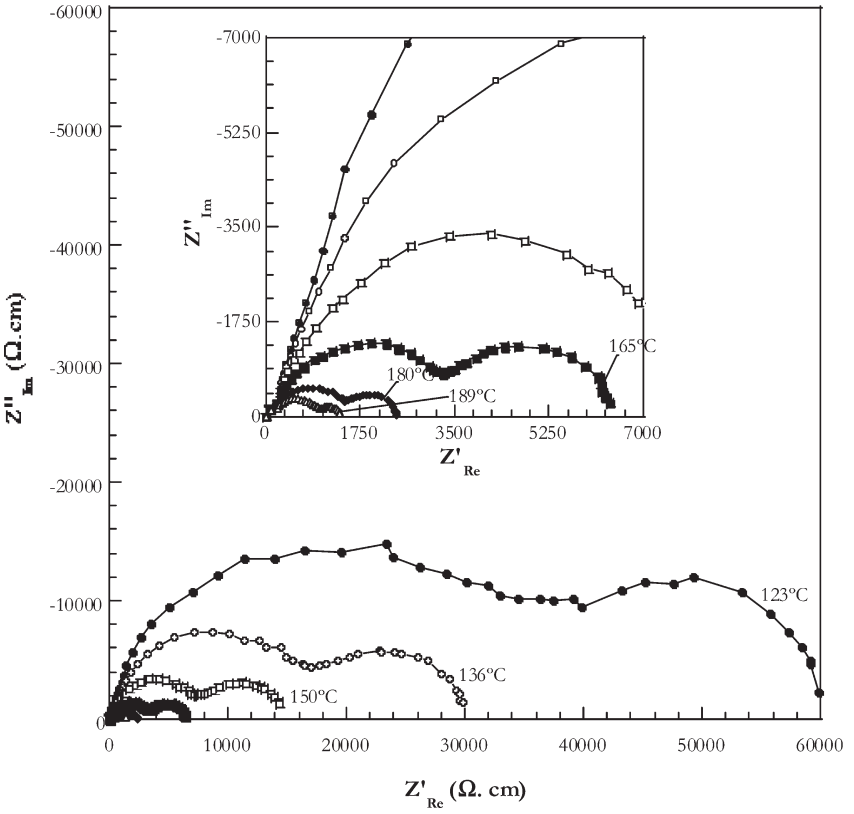

Figure 15. Thermal evolution of the Nyquist diagrams for $Li_{1.43}[Fe^{II}_{4.43}Fe^{III}_{0.57}(HPO_3)_6]\cdot 1.5H_2O$.

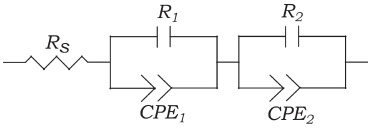

Figure 16. Equivalent circuit model used to fit the impedance spectra of $Li_{1.43}[Fe^{II}_{4.43}Fe^{III}_{0.57}(HPO_3)_6]\cdot 1.5H_2O$.

proposed by West,[30] one conduction process by a ferroelectric bulk phenomenon, together with a second process related to the resistance at the grain boundaries and/or surface layer, are observed in this compound. The ferroelectric behavior associated to the bulk conduction process might be due to the polarization caused by the charge carrier movement into the channels of the structure (mainly Li^+, but the possibility of H^+ species from water should not be discarded). Nevertheless, a detailed study of this phenomenon falls outside the scope of this work.

Conductivity increases with temperature for both processes, and from the Arrhenius plots of conductivity (shown in Figure 17), activation energies of E_A = 1.007 and 0.854 eV have been obtained, with values near 10^{-3} S cm^{-1} at 189 °C.

■ ELECTROCHEMICAL PROPERTIES: CYCLIC VOLTAMMETRY STUDY

The electrochemical behavior of the sample was analyzed by cyclic voltammetry, applying a very low scan rate (0.1 mV s^{-1}) in the range from 4 V to 1.5 V vs Li/Li^+ (see Figure 17), which is the voltage window at which reversible Fe^{2+}/Fe^{3+} redox reactions are usually found. The observed OCV for the system [$Li/LiPF_6$(EC:DMC)/phosphite] is ∼2.9 V.

Figure 18 shows the presence of two quasi-reversible processes, centered at 2.5 and 3 V (second cycle: oxidation, 2.74 and 3.12 V; reduction, 2.34 and 2.85 V). This result is in good agreement with the structural analysis revealing the existence of two crystallographic sites for the Fe atoms both occupied by Fe(II) and Fe(III). In the absence of impurities, the two observed processes will therefore correspond to the Fe(II)/Fe(III) redox reaction in two slightly different environments. This behavior is similar to that observed for [$Li_3M_2(PO_4)_3$] NASICON-type materials.[31] Their structure presents two crystallographic sites for the metal ions that have been related to the two neighboring but distinguishable processes observed in the electrochemical measurements as two voltammetric peaks.

It is also well-known that the redox potential of the Fe(II)/Fe(III) pair varies with the crystal structure and nature of the polyanion, in such a way that a stronger X−O bond weakens via the inductive effect of the covalence of the Fe−O bond, thus increasing the iron redox potential. Samples with iron and polyanions reported in the literature show values in the range of 2.5−3.6 V [i.e., 2.55 V for $LiFeAsO_4$, 2.6 and 2.8 V of $Li_3Fe_2(PO_4)_3$, 3.4 V of $LiFePO_4$, 3.6 V for $Li_xFe_2(SO_4)_3$].[32] The sample $Li_{1.43}[Fe^{II}_{4.43}Fe^{III}_{0.57}(HPO_3)_6]\cdot 1.5H_2O$, with peak potentials at 2.5 and 3 V, fitted into the cited interval with values very near to those of NASICON-type phosphates. This feature supports assignment of the processes given above and shows the similarities in the polyanion environments of this sample and $Li_3Fe_2(PO_4)_3$, although their crystal structures are quite different. Therefore, the inductive effect on the Fe−O−P system of phosphite and phosphate groups, respectively, is similar in both phases.

There is no other process appearing in the cyclic voltammetry that would indicate the presence of iron oxide secondary phases

dx.doi.org/10.1021/cm201337g |Chem. Mater. 2011, 23, 4317–4330

Table 5. (a) Values of the Resistance (R) Obtained from the Fits of the Impedance Spectroscopy (IS) Data, Values of the Resistivity (ρ), and Conductivity (σ), Calculated from the Resistance Data; and (b) Values of the CPE-T and CPE-P Parameters Obtained from the Fits of the IS Data, and Values of the Capacitance (C), Calculated from Them

(a) Resistance, Resistivity, and Conductivity Values

T (°C)	R_s (Ω)	R_1 (Ω)	ρ_1 (Ω cm)	σ_1 (Ω^{-1} cm^1)	R_2 (Ω)	ρ_2 (Ω cm)	σ_2 (Ω^{-1} cm^{-1})
123	162(18)	$2.8(1) \times 10^4$	45724	2.1870×10^{-5}	$36(2) \times 10^4$	58024	1.7234×10^{-5}
136	178(7)	$1.64(3) \times 10^4$	26453	3.7804×10^{-5}	$14.2(6) \times 10^4$	23000	4.3478×10^{-5}
150	150(7)	$7.5(7) \times 10^3$	12194	8.2009×10^{-5}	$7.3(2) \times 10^3$	11786	8.4844×10^{-5}
165	121(6)	$3.24(3) \times 10^3$	5237.5	1.9093×10^{-4}	$3.10(6) \times 10^3$	5019.2	1.9924×10^{-4}
180	92(7)	$1.40(1) \times 10^3$	2262.2	4.4205×10^{-4}	$0.95(2) \times 10^3$	1535.3	6.5132×10^{-4}
189	110(4)	$0.83(8) \times 10^3$	1339.7	7.4644×10^{-4}	$0.48(1) \times 10^3$	769.53	1.2995×10^{-3}

(b) CPE-T and CPE-P Parameters Obtained from the Fits of the IS Data, and Capacitance Values

T (°C)	CPE_1-T	CPE_1-P	C_1 (F)	CPE_2-T	CPE_2-P	C_2 (F)
123	$1.20(5) \times 10^{-9}$	0.927(9)	5.3214×10^{-10}	$2.8(4) \times 10^{-7}$	0.65(3)	2.3465×10^{-8}
136	$1.78(9) \times 10^{-9}$	0.892(9)	5.0106×10^{-10}	$1.7(3) \times 10^{-7}$	0.81(3)	3.9986×10^{-8}
150	$2.5(1) \times 10^{-9}$	0.873(9)	5.0040×10^{-10}	$1.6(3) \times 10^{-7}$	0.84(2)	4.4943×10^{-8}
165	$3.9(3) \times 10^{-9}$	0.847(8)	5.0025×10^{-10}	$1.6(2) \times 10^{-7}$	0.86(2)	4.9606×10^{-8}
180	$6.7(7) \times 10^{-9}$	0.813(8)	4.7490×10^{-10}	$3.1(4) \times 10^{-7}$	0.85(2)	7.2996×10^{-8}
189	$5.4(5) \times 10^{-9}$	0.839(8)	5.0247×10^{-10}	$9(1) \times 10^{-7}$	0.75(1)	7.4511×10^{-8}

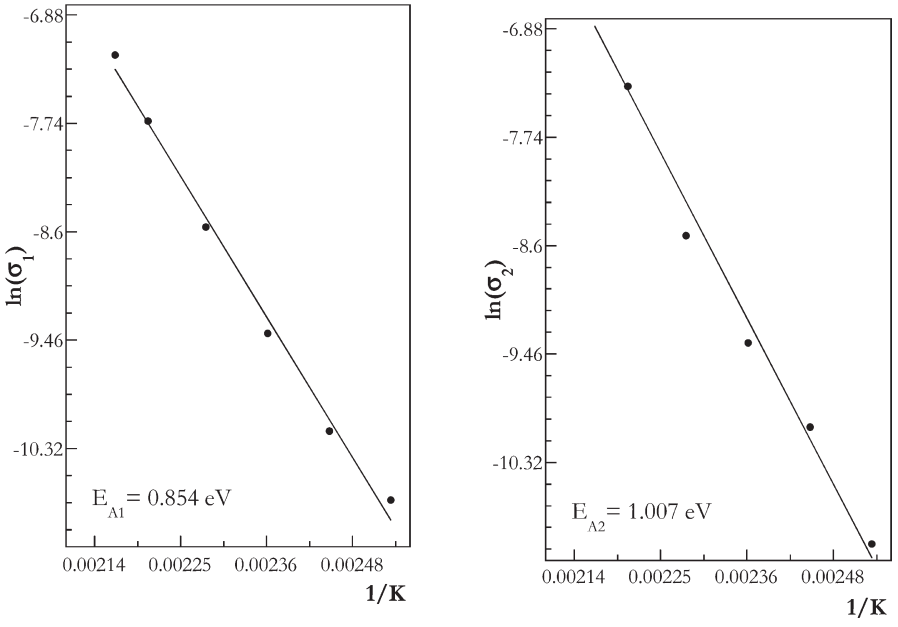

Figure 17. Arrhenius plots corresponding to the two conduction processes in $Li_{1.43}[Fe^{II}_{4.43}Fe^{III}_{0.57}(HPO_3)_6] \cdot 1.5H_2O$.

(~1.5 V) or the degradation of phosphite groups to phosphate that would occur at ~2 V vs Li/Li^+ for the $PO_4^{3-} \leftrightarrow HPO_3^{2-}$ reaction. Voltammetry measurements with a lower cutoff voltage were also performed to observe any process corresponding to the structural water in the compound, which is expected in the interval of 0.8−1.4 V vs Li/Li^+ (see Figure S1 in the Supporting Information). Therefore, the signal at 1.2 gradually shifting to higher voltage and lower intensity is ascribed to H_2O reduction, accompanied by the formation of small amounts of FeO_x characterized by a peak at 1.6 V. As for other hydrated phases, such as $Fe(PO_4).2H_2O$ polymorphs previously studied as positive electrodes for lithium batteries,[33] structural water should not hinder the Li^+ exchange capability. Below 1 V, irreversible peaks appeared in reduction, indicating the formation of metallic Fe^0 and the structural degradation of the compound.

It is also usual to find differences between the first and following cycles, because the kinetic effects affect foremost the first cycle response. However, the progressive overlapping of the two processes with cycling is more significant (Figures 18a and 18b). This could indicate a restructuring of iron octahedra toward more similar environments. Prior to cycling, the structural characterization showed that the $Fe(1)O_6$ octahedron is more

dx.doi.org/10.1021/cm201337g |*Chem. Mater.* 2011, 23, 4317–4330

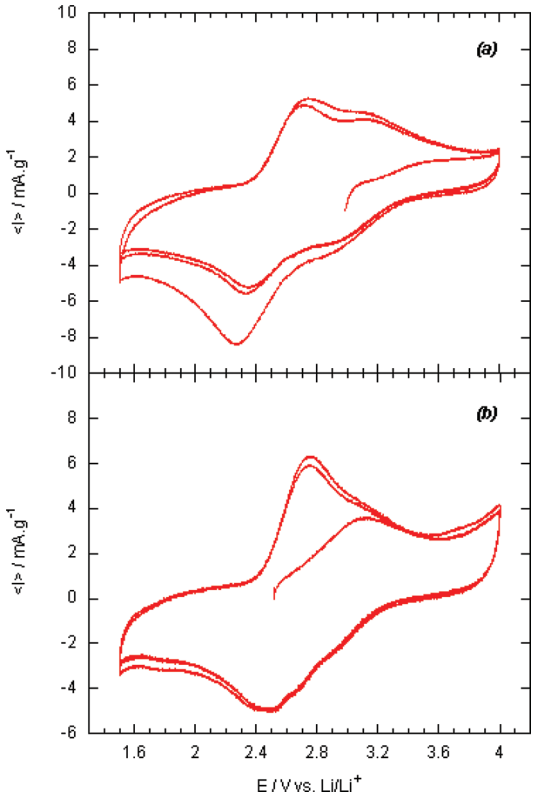

Figure 18. Cyclic voltammetry (0.1 mV s^{-1} vs Li/Li^+) of a $Li_{1.43}[Fe^{II}_{4.43}Fe^{III}_{0.57}(HPO_3)_6]\cdot 1.5H_2O$ cell, oxidizing the sample up to 4 V from OCV: (a) first three cycles and (b) three more cycles after a rest period.

distorted than $Fe(2)O_6$ with the subsequent difference between peaks observed in the voltammetry (500 mV in reduction). Therefore, the decrease in peak separation (330 mV) with cycling could indicate a reduction of the octahedral distortion to give a more symmetric environment.

In contrast with this behavior, the initial oxidation from OCV to 4 V is anomalous. Taking into account the major presence of Fe(II) in the sample (4.5:1 formula ratio), a sign of its oxidation to Fe(III) will be expected. However, a total charge of barely 61 mC was observed, whereas the following reduction processes can be clearly seen (349 mC). The oxidation charge was ~0.13 mol of Fe(II), whereas the reduction process involved 0.79 mol of Fe(III). For subsequent cycles, the total oxidation and reduction charges were the same, equivalent to ~0.49 mol of Fe. Starting from a 4.5:1 formula ratio of Fe(II):Fe(III), the observed low oxidation could be due to surface characteristics of the material, i.e., encapsulation of Fe(II) that hinders the redox reaction, but due to the water/Li^+ disorder and coordination in the channels of the structure, it can be better ascribed to the lower mobility of the lithium that must migrate outside the structure during the oxidation process.

A voltammetry with a first negative potential gradient was carried out to observe if the first reduction is also hindered in this case. In Figure 19, both reduction peaks can be clearly observed, corresponding to 0.58 mol of Fe, thus indicating that all the Fe(III) in the compound would be accessible for reaction. Therefore, the accompanying Li^+ ion insertion is easier than the deintercalation needed for the initial oxidation in this sample.

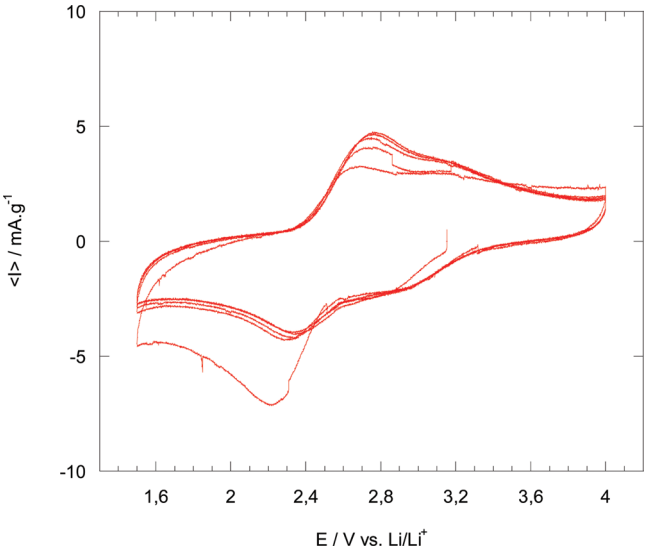

Figure 19. Cyclic voltammetry (0.1 mV s^{-1} vs Li/Li^+) of the sample $Li_{1.43}[Fe^{II}_{4.43}Fe^{III}_{0.57}(HPO_3)_6]\cdot 1.5H_2O$ performing the reduction first.

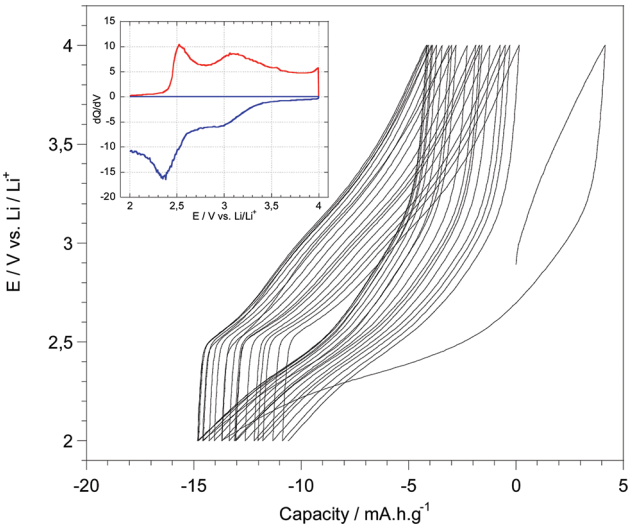

Figure 20. Galvanostatic reponse at low intensity rate (20 μA cm^{-2}; 3.6 mA g^{-1}) for the sample $Li_{1.43}[Fe^{II}_{4.43}Fe^{III}_{0.57}(HPO_3)_6]\cdot 1.5H_2O$ for 25 cycles. Inset is a plot of differential capacity (dQ/dV) vs V, showing two processes.

GALVANOSTATIC MEASUREMENTS: LITHIUM EXCHANGE CAPABILITY

The lithium exchange reaction was analyzed by galvanostatic measurements performed in the 2−4 V vs Li/Li^+ potential window (see Figure 20), in which the voltammetric measurements have shown that the Fe^{2+}/Fe^{3+} reaction occurs. The applied intensity (11 μA) was low to ensure the study of lithium reaction, corresponding to a moderate C-rate (C/13) in a lithium ion battery rate

Several intercalation/deintercalation cycles of a cell are shown in Figure 20. No clear plateau is observed, indicating that little phase separation occurs with the lithium exchange. The plot of the differential capacity (dQ/dV) vs V (inset in Figure 20) allows the distinguishing of two oxidation peaks at 2.6 and 3.1 V, in accordance with the results obtained in the voltammetries.

dx.doi.org/10.1021/cm201337g |*Chem. Mater.* 2011, 23, 4317–4330

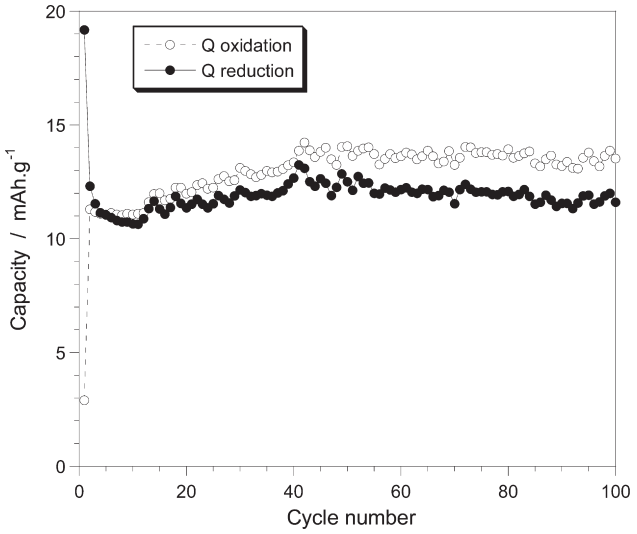

Figure 21. Cycling behavior of the sample at applied intensity of 20 μA cm^{-2}.

The stability of the sample against cycling is represented in Figure 21. This compound withstands more than 100 oxidation/reduction cycles without capacity fading, indicative of the reversible exchange of lithium along the [001] channels with only the slight restructuring of the surrounding FeO_6 octahedra discussed in the cyclic voltammetry studies. Taking into account the 1.43 mol of Li present in $Li_{1.43}[Fe^{II}_{4.43}Fe^{III}_{0.57}(HPO_3)_6]\cdot 1.5H_2O$, this compound would present a maximum theoretical specific capacity value of 50 mAh g^{-1}. From the voltammetry measurements, however, lithium in one of the crystallographic positions appears less prone to migrate, so the practical specific capacity can be expected to reduce even down to 25 mAh g^{-1} (experimental, 12 mAh g^{-1}) since the occupation factors of Li(1) and Li(2) are nearly equal.

CONCLUDING REMARKS

A new lithium−mixed-valency iron(II,III) phosphite has been synthesized under mild hydrothermal conditions. The structure is formed by layers of FeO_6 octahedra that link along the *c*-direction via phosphite groups. There are 12-membered ring channels parallel to the ***c***-axis, ca. 3 Å in diameter, where the Li cations are located, showing a positional disorder. After reaching the thermal stability limit, located at 285 °C, the destruction of the crystal structure occurs. Mössbauer data showed substitution of Fe^{2+} by Fe^{3+} in both crystallographic sites of iron. This phase is the first phosphite exhibiting a spin glass magnetic behavior. It presents ideal crystallographic and chemical features for ionic conduction and electrochemical properties. In this regard, two ionic conduction processes have been observed above 120 °C. The sample also shows reversible redox behavior due to the mixed Fe(II,III) with processes at 2.5 and 3 V vs Li/Li$^+$, coupled with a lithium extraction/insertion capability. This phase is the first phosphite polyanion-based material that shows reversible Li-ion intercalation and iron redox reaction.

ASSOCIATED CONTENT

Supporting Information. Selected hydrogen-bond contacts (Å) for the two water molecules sites O1W and O2W (Table S1). Li−O distances (Å) for the two lithium sites, Li1 and Li2 (Table S2). Voltammmetric measurement for the detection of the structural water in $Li_{1.43}[Fe^{II}_{4.43}Fe^{III}_{0.57}(HPO_3)_6]\cdot 1.5H_2O$ (Figure S1). This information is available free of charge via Internet at http://pubs.acs.org/.

AUTHOR INFORMATION

Corresponding Author

*Tel.: 0034 946012458 or 0034 945297108 (T.R.), 0034 946015523 (J.L.M.). Fax: 0034 946013500 (T.R. and J.L.M.). E-mails: teo.rojo@ehu.es or trojo@cicenergigune.com (T.R.), joseluis.mesa@ehu.es (J.L.M.).

ACKNOWLEDGMENT

This work has been financially supported by the "Ministerio de Educación y Ciencia" (MAT2010-19442, MAT2010-15375, MAT2007-66737-C02-01, MAT2007-64486-C07-05, MAT2007-60400, MAT2007/66737, and MAT2008-06542-C04) and the "Gobierno Vasco-Ayudas para apoyar las actividades de Grupos de Investigación del Sistema Universitario Vasco" (Nos. IT-177-07 and IT-312-07). U-C.C. thanks the UPV/EHU for funding. We would also like to thank L. Rodríguez and Ikerlan Technology Centre for helpful discussions, A. Lago for her kind experimental assistance with the electrochemical tests. and P. Vitoria for single-crystal X-ray diffraction measurements at low temperature and structural resolution.

REFERENCES

(1) (a) Barrer, R. M. *Hydrothermal Chemistry of Zeolites*; Academic Press: London, 1982. (b) Cheetham, A. K.; Ferey, G.; Loiseau; Thomas, T. *Angew. Chem., Int. Ed.* **1999**, *38*, 3268. (c) Thomas, J. M. *Angew. Chem., Int. Ed.* **1999**, *38*, 3628. (d) Schüth, F.; Schmidt, W. *Adv. Mater.* **2002**, *14*, 629. (e) Rao, C. N. R.; Natarajan, S.; Vidhyanathan. *Angew. Chem., Int. Ed.* **2004**, *43*, 1466. (f) Müller, A.; Reuter, H.; Dillinger, S. *Angew. Chem., Int. Ed.* **1995**, *34*, 2328.

(2) (a) Hagraman, P. J.; Hargman, D.; Zubieta, J. *Angew. Chem., Int. Ed.* **1999**, *38*, 2638. (b) Battern, S. R.; Robson, R. *Angew. Chem., Int. Ed.* **1998**, *378*, 1460. (c) Maspoch, D.; Ruiz-Molina, D.; Vaciana, J. *Chem. Soc. Rev.* **2007**, *36*, 770. (d) Clearfield, A. *Curr. Opin. Solid State Mater. Sci.* **1996**, *1*, 268. (e) Eddaoudi, M.; Moler, D. B.; Li, H.; Chen, B.; Reineke, T. M.; O'Keeffe, M.; Yaghi, O. M. *Acc. Chem. Res.* **2001**, *34*, 319. (f) Jones, W., Rao, C. N. R., Eds. *Supramolecular Organization and Materials Design*; Cambridge University Press: Cambridge, U.K., 2002.

(3) Wilson, S. T.; Lok, B. M.; Mesina, C. A.; Cannan, T. R.; Flanigen, E. D. *J. Am. Chem. Soc.* **1982**, *104*, 1146.

(4) Yu, J.; Xu, R. *Chem. Soc. Rev.* **2006**, *35*, 593.

(5) (a) Maspoch, D.; Ruiz-Molina, D.; Veciana, J. *Chem. Soc. Rev.* **2007**, *36*, 770. (b) Ferey, G. *Chem. Soc. Rev.* **2008**, *37*, 191. (c) Natarajan, S. W.; Mandal, S. *Angew. Chem., Int. Ed.* **2008**, *47*, 2. (d) Rojo, T.; Mesa, J. L.; Lago, J.; Bazan, B.; Pizarro, J. L.; Arriortua, M. I. *J. Mater. Chem.* **2009**, *19*, 1–27.

(6) Berrocal, T.; Mesa, J. L.; Pizarro, J. L.; Bazan, B.; Iglesias, M.; Aguayo, A. T.; Arriortua, M. I.; Rojo, T. *Chem. Commun.* **2008**, 4738.

(7) Tarascon, J.-M.; Armand, M. *Nature* **2001**, *414*, 359.

(8) Salah, A.A.; Jozwiak, P.; GarBarczyk, J.; Benkhouja, K. J.; Julien, C. M. *J. Powers Sources* **2005**, *140*, 370.

(9) Ramana, C. V.; Ait-Salah, A.; Utsunomiya, S.; Mauger, A.; Gendron, A. *Chem. Mater.* **2007**, *19* (22), 5319.

(10) Werner, P. E. TREOR, "Trial and Error Program for Indexing of Unknown Powder Patterns", 1984.

(11) Rodríguez Carvajal, J. FULLPROF Program. "Rietveld Pattern Matching Análisis of Powder Patterns"; Unpublished work, 1994.

(12) Oxford Diffraction, Ltd. *CrysAlisPro, v. 171.30.66*; Oxford Diffraction Ltd.: Abingdon, Oxfordshire, England, 2010.
(13) (a) Palatinus, L.; Chapuis, G. *J. Appl. Crystallogr.* **2007**, *40*, 786. (b) Spek, A. L. *Acta Crystallogr., Sect. D: Biol. Crystallogr.* **2009**, *D65*, 148.
(14) Sheldrick, G. M. *Acta Crystallogr., Sect. A: Found Crystallogr.* **2008**, *A64*, 112.
(15) Dowty, E. ATOMS V.6.0, "*A Computer Program for Displaying Atomic Structures*"; Shape Software: Kingsport, TN, 2003.
(16) Muetterties, E. L.; Guggenberger, L. J. *J. Am. Chem. Soc.* **1974**, *96*, 1748.
(17) (a) *Powder Diffraction Files Inorganic and Organic*; International Centre for Diffraction Data (ICDD): Newtowne Square, PA, 2001, File Card No. 30-0659. (b) *Powder Diffraction Files Inorganic and Organic*; ICDD: Newtowne Square, PA, 2001, File Card No. 84-0876. (c) *Powder Diffraction Files Inorganic and Organic*; ICDD: Newtowne Square, PA, 2001, File Card No. 80-1371.
(18) (a) Nakamoto, K. *Infrared and Raman Spectroscopy of Inorganic and Coordination Compounds*; John Wiley & Sons: New York, 1997. (b) Dolphin, D.; Nick, A. E. *Tabulation of Infrared Spectral Data*; John Wiley & Sons: New York, 1997.
(19) Goldman, D. S.; Rossman, G. *Am. Mineral.* **1977**, *59*, 868.
(20) Lever, A. B. P. *Inorganic Electronic Spectroscopy*; Elsevier Science Publisher B.V.: Amsterdam, 1984.
(21) Fernandez-Armas, S.; Mesa, J. L.; Pizarro, J. L.; Garitaonandia, J. S.; Arriortua, M. I.; Rojo, T. *Angew. Chem., Int. Ed.* **2004**, *43*, 977.
(22) Brand, R. A.; Lauer, J.; Heralch, D. M. *J. Phys. F: Mater. Phys.* **1983**, *13*, 675.
(23) Menil, F. *J. Phys. Chem. Solids* **1985**, *46*, 763.
(24) Tholence, J. L. *Solid State Commun.* **1980**, *35*, 113.
(25) Mauger, A.; Ferre, J.; Ayadi, M.; Nordblad, P. *Phys. Rev. B* **1988**, *37*, 9022.
(26) (a) Moorjani, K.; Coey, J. M. D. In *Magnetic Glasses*; Wolsky, S. P., Czanderna, A. W., Eds.; Methods and Phenomena, Vol. 6; Elsevier: Amsterdam, 1984. (b) Fischer, J. H.; Hertz, J. *Spin Glasses*; Cambridge University Press: Cambridge, England, 1991. (c) Mydosh, J. A. *Spin Glasses: An Experimental Introduction*; Taylor & Francis: London, 1993.
(27) (a) De Pedro, I.; Rojo, J. M.; Jubera, V.; Rodríguez Fernández, J.; Sánchez Marcos, J.; Lezama, L.; Rojo, T. *J. Mater. Chem.* **2004**, *14*, 1157. (b) de Pedro, I.; Rojo, J. M.; Pizarro, J. L.; Rodríguez Fernández, J.; Sánchez Marcos, J.; Fernández-Díaz, M. T.; Arriortua, M. I.; Rojo, T. *J. Phys.: Condens. Matter* **2006**, *18*, 3767. (c) de Pedro, I.; Rojo, J. M.; Pizarro, J. L.; Rodríguez Fernández, J.; Sánchez Marcos, J.; Fernandez Diaz, M. T.; Arriortua, M.; Rojo, T. *J. Mater. Chem.* **2007**, *17*, 3915.
(28) (a) Rojo, J. M.; Mesa, J. L.; Lezama, L.; Pizarro, J. L.; Arriortua, M. I.; Rodriguez Fernández, J.; Barberis, G. E.; Rojo, T. *Phys. Rev. B* **2002**, *66*, 094406.
(29) Rojo, J. M.; Pizarro, J. L.; Rodríguez-Fernández, J.; Greneche, J. M.; Arriortua, M. I.; Fenández-Díaz, M. T.; Rojo, T. *J. Mater. Chem.* **2003**, *13*, 1723.
(30) West, A. R. *Solid State Chemistry and Its Applications*; John Wiley & Sons: New York, 1984; Chapter 15.
(31) Anderson, A. S.; Kalska, B.; Eyob, P.; Aernout, D.; Häggström, L.; Thomas, J. O. *Solid State Ionics* **2001**, *140*, 63.
(32) (a) Masquelier, C. *Lithium Batteries: Science and Technology*; Nazri, G., Pistoia, G., Eds.; Kluwer Academic Publishers: Norwell, MA, 2004. (b) Goodenough, J. B. *Lithium Ion Batteries*; Wakihara, M., Yamamoto, O., Eds.; Kodansha: Tokyo, 1998; Chapter 1.
(33) Reale, P.; Scrosati, B.; Delacourt, C.; Wurm, C.; Morcrette, M.; Masquelier, C. *Chem. Mater.* **2003**, *15* (26), 5051.